Article

Polarization entanglement enabled by orthogonally stacked van der Waals NbOCl$_2$ crystals

Check for updates

Qiangbing Guo [1,2,10] ✉, Yun-Kun Wu[3,4,5,10], Di Zhang[6,7,10], Qiuhong Zhang[8], Guang-Can Guo[3,4,5], Andrea Alù [6,9], Xi-Feng Ren [3,4,5] ✉ & Cheng-Wei Qiu [1,2] ✉

Polarization entanglement holds significant importance for photonic quantum technologies. Recently emerging subwavelength nonlinear quantum light sources, e.g., GaP and LiNbO$_3$ thin films, benefiting from the relaxed phase-matching constraints and volume confinement, have shown intriguing properties, such as high-dimensional hyperentanglement and robust entanglement anti-degradation. Van der Waals (vdW) NbOCl$_2$ crystal, with strong optical nonlinearities, has emerged as a potential candidate for ultrathin quantum light sources. However, polarization entanglement is inaccessible in the NbOCl$_2$ crystal due to its unfavorable nonlinear susceptibility tensor. Here, by leveraging the twist-stacking degree of freedom inherently in vdW systems, we showcase the preparation of polarization entanglement and quantum Bell states.

An entangled quantum light source serves as the foundation for various quantum technologies, including secure communications, quantum computing, quantum metrology and sensing, quantum imaging, as well as testing fundamental principles of quantum mechanics[1–7]. A second-order nonlinear ($\chi^{(2)}$) process, referred to as spontaneous parameter down conversion (SPDC), is the workhorse for generating such entangled quantum light states. Conventionally, bulky $\chi^{(2)}$ crystals (such as BBO, KDP, KTP) are used for sufficient SPDC efficiency[2–4]. Recently, on-chip waveguides (e.g., periodically poled lithium niobate, PPLN) and microresonators (e.g. AlN microring, LN microdisk) have been developed and shown promise as bright SPDC sources[8–12], spurred by the advances in the fabrication and processing techniques of LN and AlN thin films. It is noted that both these conventional bulk crystals and on-chip waveguides/resonators adopts a light-matter interaction length significantly longer than their coherent lengths, indicating a phase-matching condition is indispensable for high efficiency or brightness[13].

Very recently, subwavelength thin SPDC sources have attracted broad attentions due to intriguing new features resulting from the relaxation of phase-matching constraints. These features include ultrabroad frequency and angular spectra, ultrashort correlation times and distances, as well as giant degrees of time-frequency and position-momentum entanglement[14–17]. This relaxation in subwavelength films enhances flexibility in engineering entangled quantum light states, essential for quantum optics and related technologies. For example, Santiago-Cruz et al. generated complex quantum states using a subwavelength semiconductor film with designed high-quality optical resonances[18], an

[1]Department of Electrical and Computer Engineering, National University of Singapore, Singapore, Singapore. [2]Centre for Advanced 2D Materials and Graphene Research Centre, National University of Singapore, Singapore, Singapore. [3]CAS Key Laboratory of Quantum Information, University of Science and Technology of China, Hefei, China. [4]CAS Synergetic Innovation Center of Quantum Information and Quantum Physics, University of Science and Technology of China, Hefei, China. [5]Hefei National Laboratory, University of Science and Technology of China, Hefei, China. [6]Photonics Initiative, Advanced Science Research Center, City University of New York, New York, NY, USA. [7]The Key Laboratory of Weak-Light Nonlinear Photonics, Ministry of Education, School of Physics and TEDA Applied Physics Institute, Nankai University, Tianjin, China. [8]School of Chemistry and Materials Science, Hangzhou Institute for Advanced Study, University of Chinese Academy of Sciences, Hangzhou, China. [9]Physics Program, Graduate Center, City University of New York, New York, NY, USA. [10]These authors contributed equally: Qiangbing Guo, Yun-Kun Wu, Di Zhang. ✉e-mail: qbguo90@hotmail.com; renxf@ustc.edu.cn; chengwei.qiu@nus.edu.sg

approach not feasible with phase-matching engineered bulk crystals or on-chip waveguides/microresonators.

2D van der Waals (vdW) materials, known for their strong optical nonlinearities, in addition to their ease of vdW integration with various photonic structures[19–21]. These features make them a desirable platform for subwavelength SPDC sources. The high nonlinearity is beneficial for nonlinear devices with reduced interaction volume, while the ease vdW coupling with photonic structures facilitate the development of high-performance and multifunctional SPDC sources.

More importantly, as a unique enabling feature due to weak vdW bonding, twist engineering has been well established as a new knob for shaping and inducing exotic material properties, including superconductivity, correlated insulators, moiré excitons, topological phonon polariton transitions, optical nonlinearities, among many others[22–25]. For example, interlayer twist was recently shown to induce new second- and third-harmonic generation processes in 2D WS$_2$ via engineering of the atomic symmetry[26], and single photon emission from interlayer excitons in trapped moiré potential has been confirmed[27]. For SPDC processes in subwavelength film, the polarization configuration of the generated photon pairs is dictated by the nonlinear tensor structure[14]. VdW twist engineering is expected to potentially provide a novel approach to manipulate two-photon polarization states, which, however, has not yet been explored.

Very recently, NbOCl$_2$ has been identified as a vdW crystal with fairly high nonlinearity compared to other vdW materials and showcased the first ultrathin vdW SPDC source[28], offering a promising vdW SPDC platform at the nanoscale. However, as we have systematically revealed in this work, NbOCl$_2$ crystal intrinsically lacks favorable susceptibility tensor for polarization entanglement that is pivotal for practical qubit encoding[1,5,6,14,29,30]. To extend the function of this new vdW SPDC platform, we have further successfully constructed polarization-entangled quantum states by resorting to NbOCl$_2$ vdW bilayer orthogonal stacks. This presents a methodology for developing versatile, controllable, and compact vdW entangled quantum sources. Our work also implies vdW stack engineering can be a new knob for manipulating entangled quantum light states, facilitating an avenue to go further beyond the restrictions imposed by the intrinsic nonlinear tensor of natural materials and may provide higher freedom in engineering quantum states.

Results

Characterization of nonlinear tensor elements

As NbOCl$_2$ crystal adopts a C2 symmetry[28], its second-order nonlinear susceptibility tensor can be represented as a 3 × 6 matrix

$$\chi_{ijk}^{(2)} = \begin{bmatrix} 0 & 0 & 0 & \chi_{abc}^{(2)} & 0 & \chi_{aab}^{(2)} \\ \chi_{baa}^{(2)} & \boldsymbol{\chi_{bbb}^{(2)}} & \boldsymbol{\chi_{bcc}^{(2)}} & 0 & \chi_{bac}^{(2)} & 0 \\ 0 & 0 & 0 & \boldsymbol{\chi_{cbc}^{(2)}} & 0 & \chi_{cab}^{(2)} \end{bmatrix}. \quad (1)$$

The second-order nonlinear processes are essentially generated by the interaction between the electric fields of light with the nonlinear polarization described by this $\chi^{(2)}$ tensor. Each tensor element corresponds to a specific combination of polarization directions and interactions within the material, dictating the efficiency and characteristics of the resulting nonlinear processes.

To gain deeper insights into the $\chi^{(2)}$ tensor elements, we performed polarization-resolved second harmonic generation (SHG) measurements in a transmission configuration (Fig. 1a, b). Note that normal incidence onto the crystallographic basal plane (orthogonally defined by the b- and c-axes) is employed throughout this work (Fig. 1b). In this pump geometry, the primary tensor elements
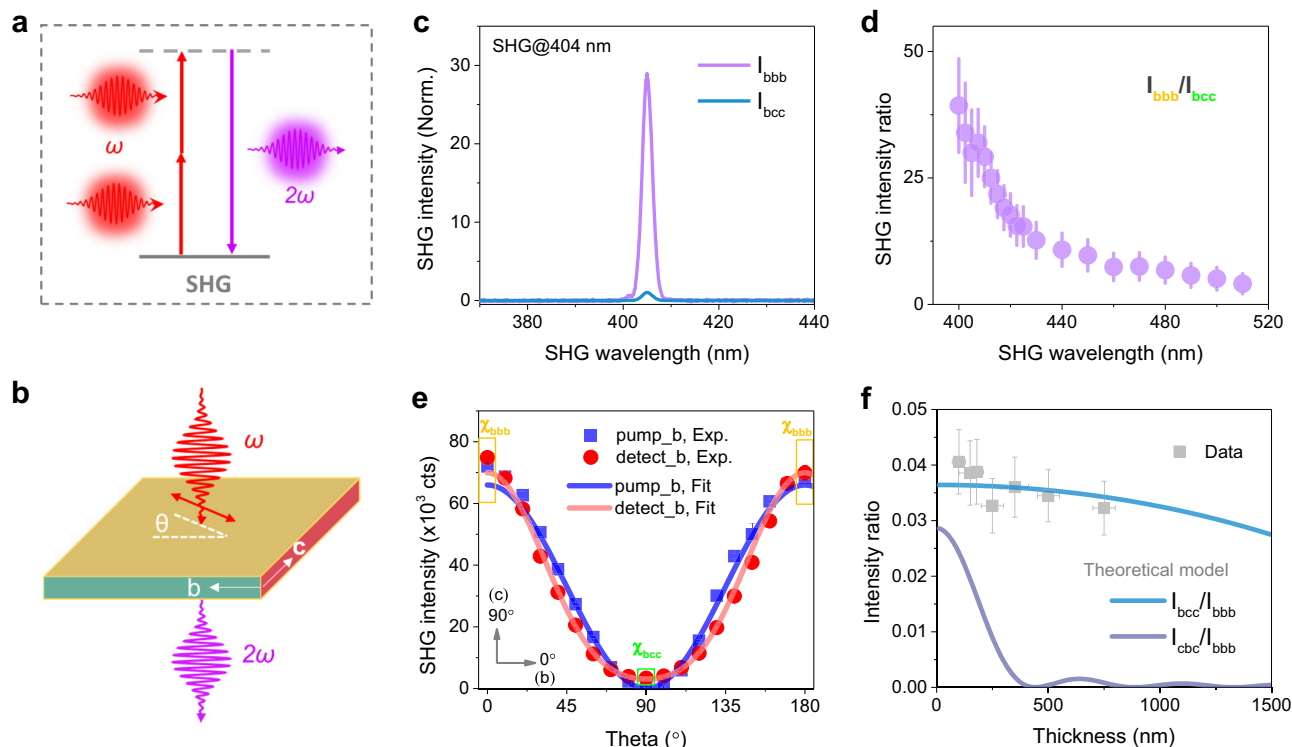
Fig. 1 | Characterization of nonlinear tensor elements through polarization-dependent SHG. Schematic illustration of the SHG process (**a**) and the experimental configuration (**b**). **c** Typical SHG spectra when pumped at 808 nm. **d** Wavelength-dependent SHG intensity ratio between the $\chi_{bbb}^{(2)}$- and $\chi_{bcc}^{(2)}$-defined processes. **e** Azimuthally dependent SHG intensity by varying pump polarization. More details about the fitting can be found in Supplementary Section S1. **f** Thickness dependence of nonlinear intensity ratios. The solid lines are modeling results based on the nonlinear tensor, while the dots are experimental results which are well consistent with the modeling. Error bars represent standard deviations from five measurements.
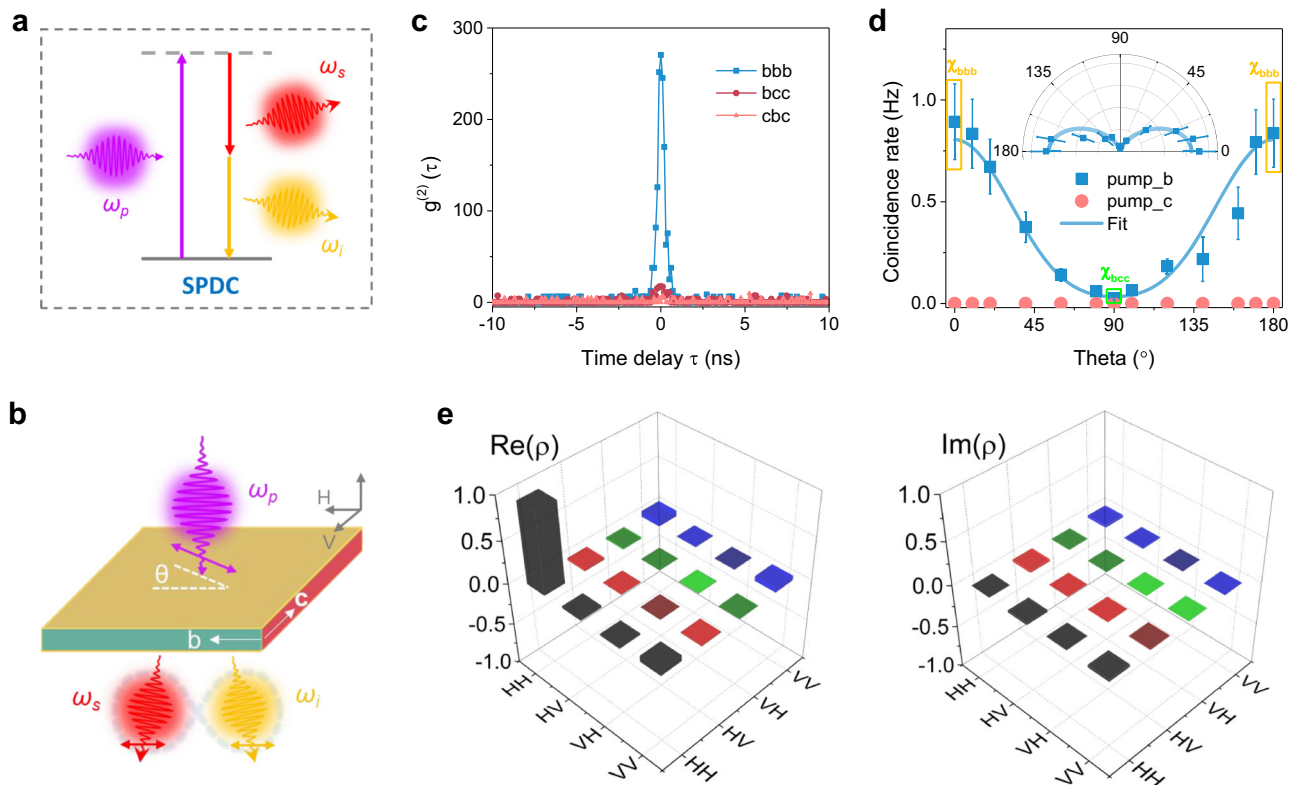
Fig. 2 | Polarization-dependent SPDC and quantum-state tomography in single NbOCl₂ flakes. Schematic illustration of SPDC process (**a**) and experimental configuration (**b**). **c** Normalized two-photon temporal correlation functions of three processes in a NbOCl₂ flake of ~200 nm thick under a pump power of ~1 mW with a 404-nm continuous-wave laser. Singal is filtered by a bandpass filter with a central wavelength of 810 nm and a full width at half maximal of 10 nm. **d** Polarization-dependent photon-pair coincidence rate. Inset is a presentation in polar coordinates. **e** Experimentally measured polarization density matrices for 45°-polarized pump. Error bars represent standard deviations from five measurements.

governing the nonlinear processes are $\chi^{(2)}_{bbb}$, $\chi^{(2)}_{bcc}$ and $\chi^{(2)}_{cbc}$ (highlighted above in bold). Specifically, $\chi^{(2)}_{bbb}$ ($\chi^{(2)}_{bcc}$) defines the processes with pump polarized along the *b*-axis (*c*-axis) and emission polarized along the *b*-axis; $\chi^{(2)}_{cbc}$ defines the processes with pump polarized along the *b*- and *c*-axes and emission polarized along the *c*-axis.

As shown in Fig. 1c, with an 808-nm pump, the SHG intensity defined by $\chi^{(2)}_{bbb}$ (I_{bbb}) is significantly larger than that defined by $\chi^{(2)}_{bcc}$ (I_{bcc}). The wavelength-dependent SHG intensity ratio of these two processes (I_{bbb}/I_{bcc}) is shown in Fig. 1d. It is evident that the nonlinear process associated with $\chi^{(2)}_{bbb}$ is stronger than the others under normal pump conditions, gaining greater dominance at shorter wavelengths within the spectral range considered here.

To comply with the following SPDC experiments, we focus on the SHG process at 404 nm (with an 808-nm pump) hereinafter. More detailed azimuthal dependencies of SHG intensity under different polarization configurations were measured (Fig. 1e; see Supplementary Fig. S1 for additional data). These results were fitted using theoretical models to derive a tensor element ratio of $\chi^{(2)}_{bbb}/\chi^{(2)}_{bcc} \sim 4.65$ (the calculation method is detailed in Supplementary Section S1). To account for the thickness dependence of the nonlinear processes, we modeled the nonlinearity intensity ratios (I_{bcc}/I_{bbb} and I_{cbc}/I_{bbb}) based on this derived tensor element ratio (more details and analysis can be found in Supplementary Fig. S2). The corresponding results are presented in Fig. 1f, where the $\chi^{(2)}_{bbb}$ process exhibits significant dominance over the considered thickness range, and the weight gets higher with thickness. The modeled results are well-supported by the experimental data points presented in Fig. 1f. Notably, the $\chi^{(2)}_{cbc}$-defined process is very low and significantly decreases with thickness (see detailed analysis in Supplementary Fig. S2).

SPDC process in single NbOCl₂ flakes

SPDC is a $\chi^{(2)}$ process that can be seen as the time-reversal of SFG (Fig. 2a), dictated by the same nonlinear tensor as in the SHG/SFG processes[31]. Therefore, the above-mentioned three tensor elements also define the main SPDC processes in transmission configuration as adopted in the following SPDC experiments (Fig. 2b). As shown in Fig. 2c, when pumped by a 404-nm continuous-wave laser in a Hanbury-Brown-Twiss interferometer, an obvious two-photon correlation peak with a $g^{(2)}(0)$ value over 260 could be observed with the pump and detection both polarized along the *b*-axis (i.e., $\chi^{(2)}_{bbb}$-defined process). This is a strong indicator for the generation of correlated photons, as uncorrelated photons result in accidental coincidences with no peak over delay time. Moreover, the inverse pump-power dependence of $g^{(2)}(0)$ value and the linear pump-power dependence of coincidence rates (Supplementary Fig. S3), as well as the two-photon de Broglie wavelength measurement (Supplementary Fig. S4), further unambiguously confirms the SPDC nature[13,15,18,29–32]. Notably, the photoluminescence signal in spectral region around 808 nm (i.e., the degenerate SPDC wavelength, see Supplementary Fig. S5) is very weak, which underpins the measured high $g^{(2)}(0)$ value at a low pump power of ~1 mW.

By contrast, much weaker peak ($g^{(2)}(0)$ ~ 10) is with the $\chi^{(2)}_{bcc}$-defined process and no obvious peak with the $\chi^{(2)}_{cbc}$-defined one under the same pump power. Therefore, the $\chi^{(2)}_{bbb}$-defined process is also the dominating one in SPDC, with a small contribution from $\chi^{(2)}_{bcc}$-defined one and almost no contribution from $\chi^{(2)}_{cbc}$-defined one. Further polarization-dependent coincidence rates were measured (Fig. 2d), which clearly indicates a strong polarization-dependence and is consistent with the above SHG analysis.
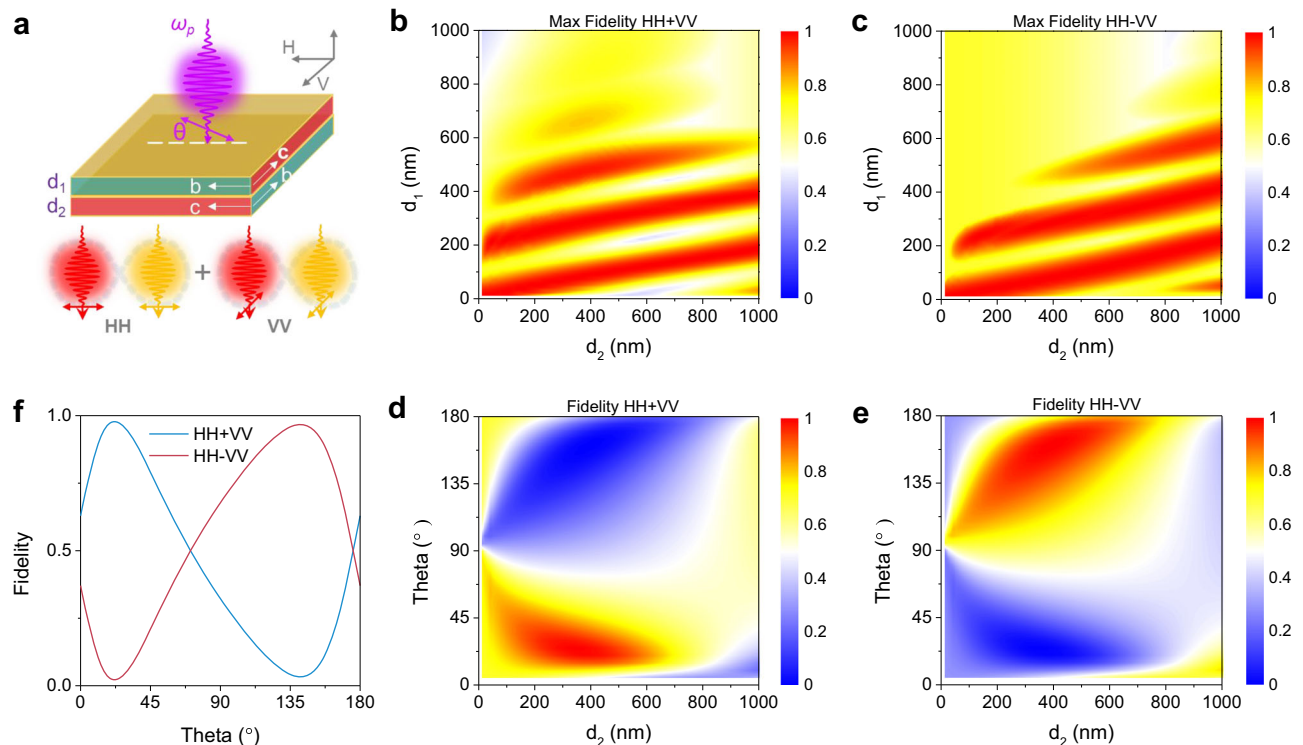
Fig. 3 | Designable and tunable polarization entanglement with NbOCl₂ bi-layer orthogonal stacks. a Schematic illustration of the geometry of the orthogonally twisted vdW bi-layer stack. d_1 (d_2) is the thickness of the first (second) crystal layer encountered by the incident pump. θ is the pump polarization angle defined against the crystallographic b-axis of the first crystal layer. **b, c** Calculated maximal fidelity in (d_1, d_2) parametric space, with two Bell states, $|\Phi^+\rangle = 1/\sqrt{2}(|HH\rangle + |VV\rangle)$ (HH + VV) and $|\Phi^-\rangle = 1/\sqrt{2}(|HH\rangle - |VV\rangle)$ (HH − VV), respectively. Each point in the parametric spaces represents the maximal fidelity that can be obtained by scanning the pump polarization angle θ. **d, e** Calculated fidelity with the two Bell states in (d_2, θ) parametric space with d_1 fixed at 80 nm. **f** Dependence of fidelity on pump polarization angle for the bi-layer stack case with d_1 = 80 nm and d_2 = 260 nm.

To gain a comprehensive picture of the polarization state of generated photon pairs in a single NbOCl₂ flake, we performed polarization tomographic measurement on a NbOCl₂ flake. As shown in Fig. 2e, when pumped with a polarization of 45° (against the b-axis), the polarization state of the generated photon pairs exhibits an HH state (H denotes the polarization along the b-axis) with a fidelity of 0.95 ± 0.02. Additional tomography results with a pump polarization of 0° could be found in Supplementary Fig. S6, where the polarization of generated photon pairs has the same HH state. In other words, the polarization state of the generated photon pairs exhibits an HH state regardless of the pump polarization. Therefore, the generated photon pairs in single NbOCl₂ flakes are not polarization-entangled as limited by its crystal symmetry and thus nonlinear susceptibility tensor structure.

Designable and tunable polarization entanglement with NbOCl₂ bi-layer orthogonal stacks

Given that polarization entanglement is pivotal for various quantum technologies[1,5,6,14,29–32], the capability to generate polarization-entangled quantum states becomes a crucial step forward for such novel vdW SPDC sources. In principle, polarization entanglement can be obtained utilizing crystals with favorable nonlinear tensors[33,34]. For example, GaP and 3R-MoS₂ were recently demonstrated to generate polarization-entangled Bell states due to their cross-polarized nonlinear tensors[29,35]. While those materials have intrinsic access to polarization entanglement guaranteed by specific crystal symmetry, the suitable nonlinear tensor types are essentially limited by available natural crystals, let alone the additional limitations imposed by their low nonlinearity (Supplementary Section S6). As compared and discussed in Supplementary Section S7, NbOCl₂ exhibits superior nonlinearity over GaP and 3R-MoS₂ thin films and conventional bulk

crystals. Moreover, the SPDC efficiency in NbOCl₂ is also orders of magnitude higher than in the GaP thin-film and 3R-MoS₂ vdW SPDC sources (Supplementary Table S1). It would be ideal if polarization entanglement could be generated with this high-nonlinearity platform.

As discussed above, the generated photon pairs from a single flake remain a HH polarization state, regardless of pump polarization, as dictated by the fixed nonlinear tensor. It is natural to consider that if two pieces of crystals are stacked in an orthogonally twisted geometry (Fig. 3a), a polarized pump with a non-zero angle (θ) will down-convert in either crystal and these two possible SPDC processes will coherently superpose with one another as the spatial modes for the emitted photon pairs are indistinguishable for the stacked crystals[5,6]. As a result, this offers an opportunity to access controllable polarization states of the generated photon pairs through an elaborate combination of the geometry parameters (d_1, d_2, and θ, as defined in Fig. 3a). In principle, the degree of polarization entanglement can be well controlled by manipulation of the weight balance between two paths (HH or VV, see Fig. 3a). Specifically, maximally entangled Bell states can be prepared when the down-conversion occurs equally in either crystal.

We firstly developed a theoretical model to describe the effect of the geometry parameters of bi-layer stack on the polarization states of the generated photon pairs (see details in section "Methods"). The fidelity with two target Bell states (maximally entangled), i.e., $|\Phi^+\rangle = 1/\sqrt{2}(|HH\rangle + |VV\rangle)$ and $|\Phi^-\rangle = 1/\sqrt{2}(|HH\rangle - |VV\rangle)$, respectively, is presented in Fig. 3b–e to reflect the two-photon polarization states. A fidelity value of 1 means a perfect Bell state ($|\Phi^+\rangle$ or $|\Phi^-\rangle$). Specifically, in the two-dimensional (d_1, d_2) parametric space, the mapping of available maximal fidelity with the two Bell states are shown in Fig. 3b, c, respectively, where each point means the maximal fidelity value that can be obtained with the indicated thickness combination by
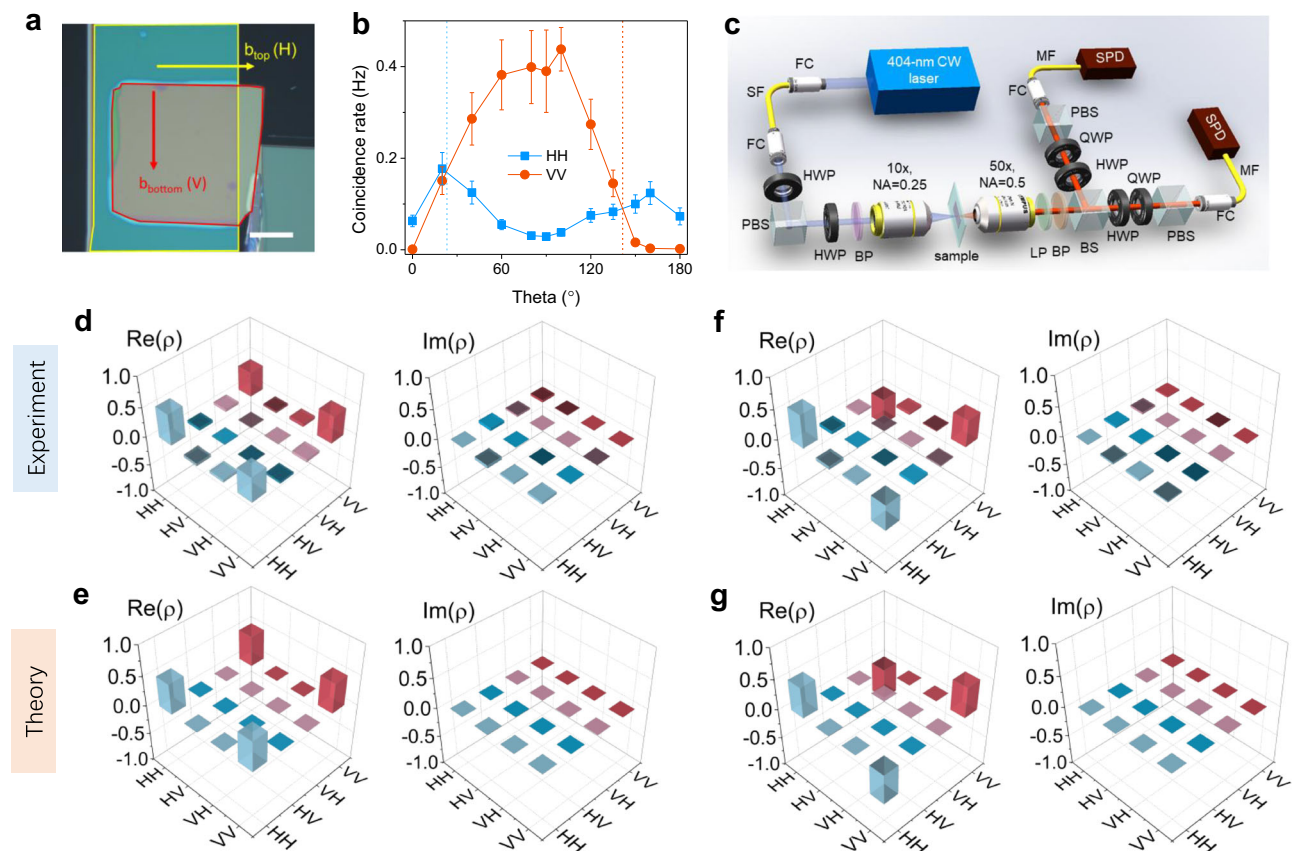
Fig. 4 | Experimental demonstration and Bell state construction with vdW bi-layer orthogonal stacks. a Optical image of a fabricated orthogonal vdW stack. d_1 ~ 80 nm, d_2 ~ 260 nm. Scar bar, 25 μm. **b** Coincidence rate of two paths (HH and VV) as a function of pump polarization angle. Error bars represent standard deviations from three measurements. **c** Illustration of the optical setup for polarization quantum state tomography. FC fiber coupler, SF single-mode fiber, PBS polarizing beam splitter, HWP half-wave plate, QWP quarter-wave plate, BP band-pass, LP long pass, BS polarization-independent beamsplitter, SF single-mode fiber, MF multimode fiber, SPD single-photon detector. Experimentally measured polarization density matrices ρ for pump polarization angle θ of 25° (**d**) and 140° (**f**), respectively. The excitation power incident on samples is ~4 mW. Theoretical density matrices for two Bell states, i.e., $|\Phi^+\rangle = 1/\sqrt{2}(|HH\rangle + |VV\rangle)$ (**e**) and $|\Phi^-\rangle = 1/\sqrt{2}(|HH\rangle - |VV\rangle)$ (**g**), respectively.

scanning the pump polarization angle from 0° to 180°. Figure 3d, e shows the fidelity value in the (d_2, θ) space, which represent the available fidelity by adjusting d_2 and θ when d_1 is fixed (tunability also exists in the (d_1, θ) space when d_2 is fixed). It is noted that the generated polarization states exhibit high design freedom with the thickness combination (Fig. 3b, c) and high tunability with pump polarization angle (Fig. 3d, e), which is also reflected in the highly controllable degree of polarization entanglement as evidenced by the mapping of concurrence with the geometry parameters in Supplementary Section S8. These widely accessible entangled states are of fundamental interests for experimental tests of quantum mechanics[36–38], as well as of technological relevance for enhanced quantum sensing, metrology, and simulation due to being more robust to certain types of noise and decoherence[39–42].

More importantly, the pump polarization angle θ could serve as a post-fabrication knob for tuning the polarization entanglement states, i.e., when stacks are fabricated (d_1 and d_2 are fixed). Take the stack case (d_1 = 80 nm, d_2 = 260 nm) as an example, the fidelities with both Bell states can be widely tuned between zero to unity by simply controlling the pump polarization (Fig. 3f), facilitating a facile access to tunable polarization-entangled states. In addition, switching between the two Bell states could be achieved by adjusting the pump polarization angle.

Experimental demonstration and construction of Bell states
As proof-of-concept demonstrations, we firstly fabricated a bi-layer stack (d_1 ~ 80 nm, d_2 ~ 260 nm) by picking up two exfoliated flakes of

target thickness and assembling them into an orthogonal stack with all-dry transfer technique (Fig. 4a, see section "Methods" for details). To gain an insight into the pump-polarization-dependent polarization state of the generated photon pairs, we measured the coincident rates along the HH and VV paths (Fig. 3a), respectively, by scanning the pump polarization angle from 0° to 180°. The results are shown in Fig. 4b, which indicates the variation of generated photon pairs with pump polarization in the two polarization paths and balances can be reached at ~25° and ~140°, respectively. This is well consistent with the modeled results shown in Fig. 3f, where maximally entangled Bell states could be accessed near these balanced pump-polarization angles.

To reconstruct the polarization state of the generated photon pairs, polarization tomographic measurements were conducted (Fig. 4c and see section "Methods" for more details). The density matrix ρ of the polarization state can be derived by projecting into 16 different basis states. As shown in Fig. 4d, the reconstructed density matrix with a pump polarization angle of 25° is presented and its fidelity with the $|\Phi^+\rangle = 1/\sqrt{2}(|HH\rangle + |VV\rangle)$ Bell state (Fig. 4e) is derived to be 0.91 ± 0.02 (see Supplementary Section S9 for more details). Besides, the reconstructed density matrix with a pump polarization angle of 140° is presented in Fig. 4f and its fidelity with the $|\Phi^-\rangle = 1/\sqrt{2}(|HH\rangle - |VV\rangle)$ Bell state (Fig. 4g) is derived to be 0.92 ± 0.03. These results align well with the modeled ones (Fig. 3f).

Furthermore, additional stacks with different thickness combinations were fabricated and their polarization entanglement states

were measured, of which the reconstructed polarization density matrices are presented in Supplementary Section S10. It is noted that polarization-entangled Bell states can be obtained by varying thickness combinations and pump polarization, as well described by the developed theoretical model.

Discussion

In conclusion, we have demonstrated the generation of polarization-entangled quantum light states based on bi-layer orthogonal stacks of NbOCl$_2$ crystal, a recently discovered high-nonlinearity $\chi^{(2)}$ vdW crystal without inherent polarization entanglement. In addition, we have successfully constructed polarization-entangled Bell states with fidelities >0.9. Our work not only provides a novel subwavelength polarization-entangled photon-pair source with high designability and tunability, but also introduces a methodology for constructing polarization-entangled quantum light states at the nanoscale from crystals inherently lacking favorable susceptibility tensor for polarization entanglement, which has the potential to significantly expand the toolbox for engineering the two-photon polarization entanglement states.

While we present a proof-of-concept demonstration, the fidelity of the polarization-entangled Bell states can be further enhanced by more precise control of sample thickness, stacking angle, and pump polarization angle. Exciting opportunities are also anticipated to emerge in creating and manipulating quantum light states through interfacing this vdW platform with cavity photonics and metaoptics[43–45], in light of the facile vdW integration with various photonic structures and twist-stacking degree of freedom demonstrated in this work.

As a novel platform for engineering photon-pair states at the nanoscale, greater designability and tunability with this twistable vdW platform is expected. For example, while we have demonstrated bi-layer orthogonal stacks, additional possibilities could be accessible by employing arbitrary twist angles and by resorting to tri-layer stacks, as shown and discussed in Supplementary Section 11. In addition, arbitrary qutrit states could also be generated with tri-layer stacked structures (see Supplementary Fig. S13 for details), underpinning an avenue towards the preparation of complex quantum states at the nanoscale that are challenging for a natural $\chi^{(2)}$ crystal with a fixed nonlinear tensor[30,46].

Methods

Crystal synthesis and characterizations

The single crystals were synthesized by chemical vapor transport as detailed in our recent paper[26]. Nb$_2$O$_5$, NbCl$_5$ and Nb powders in stoichiometric ratio were first thoroughly mixed and sealed in an evacuated quartz tube, which was then heated in a two-zone furnace with the reaction (growth) region kept at 500–600 °C (300–400 °C) for 5 days. Single crystals were obtained by slow cooling to room temperature at a rate of about 5 °C h^{-1}. The crystalline phase was confirmed with X-ray diffraction (Rigaku D/MAX 2550/PC with Cu Kα X-rays). Atomic force microscopy (Bruker Dimension Fast Scan in tapping mode) was used to identify the thickness of exfoliated flakes.

Sample fabrication

Samples were directly exfoliated onto quartz slides (20 mm × 20 mm × 0.5 mm), using traditional tape exfoliation method, for SHG and SPDC experiments on single flakes. For twisted stack samples, two flakes were initially exfoliated onto a quartz slide and a polydimethylsiloxane (PDMS) film, respectively. Subsequently, the selected flake on PDMS was transferred onto the other selected flake on quartz using an all-dry transfer method within a glovebox. Note that the exfoliated NbOCl$_2$ flakes, both on quartz and PDMS, exhibit highly anisotropic features facilitating

the identification of crystallographic axes and control of twist angles.

SHG experiment

The SHG experiments were conducted in transmission geometry with the experimental setup illustrated in Supplementary Fig. S1a. A tunable femtosecond laser (Coherent Chameleon Ultra, pulse width: 140 fs; repetition frequency: 80 MHz) was used as the pump source. A half-wave plate (HWP) before coupling into the fiber is used to control the pump power. Then the pump is coupled into a single-mode fiber (SF) and modulated to different linear polarizations with a polarization beam splitter (PBS), an 808-nm HWP. A long-pass (LP) filter (at 700 nm) is used to remove possible noise generated in fiber. The pump light is focused onto the sample by an objective (10 × , N.A. = 0.25) and the generated SHG signal is collected by another objective (10×, N.A. = 0.25). The SHG signal is projected into different linear polarizations with a HWP and a PBS. After removing the pump light by a short-pass filter, the SHG photons are coupled into an SF and recorded by single photon detector (SPD, PerkinElmer, SPCM-AQRH-15-FC). Spectrum was measured using a spectrometer (Princeton Instruments, SP2500) cooled by liquid nitrogen. All the experiments were operated at room temperature under ambient conditions and there is no noticeable change with these exfoliated flakes during regular experimental measurements. A detailed study of the stability of exfoliated flakes can be found in a recent work[47].

Biphoton correlation measurements

The two-photon correlation properties were recorded with the setup illustrated in Supplementary Fig. S3a. The pump light from a 404-nm continuous-wave laser (Toptica, DL Pro) is coupled into an SF, followed by modulation into different linear polarizations using a PBS and an HWP. The HWP before coupling into SF is used to control the pump power, while the band-pass (BP, Thorlabs, FBH405-10) after the first PBS is used to remove the possible noise generated in fiber. The pump is focused onto the sample with a 10× objective (N.A. = 0.5). After removing the pump light with an LP filter (at 700 nm) and a BP filter (Thorlabs, FBH810-10), the signal and idler photons are projected into the same various linearly polarizations with an HWP and a PBS. Finally, signal and idler photons are coupled into a same multimode fiber (MF) and separated by the fiber beam splitter (FBS, splitting radio 50:50, Thorlabs, TG625R5F1A), followed by recording by two SPDs (PerkinElmer, SPCM-AQRH-15-FC) respectively. A Time-Correlated Single Photon Counting (TCSPC) module (qutools quTAG) is used to calculate the second-order correlation function and the coincidence of the biphotons.

Polarization quantum state tomography

The experimental setup for quantum state tomography is illustrated in Fig. 4c. The pump source and focusing process are the same with that of above biphoton correlation experiments. While in this case, the signal and idler photons are separated by a polarization-independent beamsplitter (BS, splitting ratio 50:50) and individually projected into different polarization basis with a sequence of HWP, quarter-wave plate (QWP) and a PBS. This is followed by coupling the SPDC photons into MFs, detecting by SPDs and calculating the coincidence by TCSPC.

Simulations of polarization-entangled states in twisted vdW stacks

The quantum state of photon pairs generated at $z = z_0$ by SPDC could be represented as[28,48–51]:

$$\left| \psi\left(\theta, \alpha_j, z_0\right) \right\rangle = \sum_{lmn} \zeta_{lmn}\left(\theta, \alpha_j, z_0\right) \hat{a}_{i,m}^\dagger \hat{a}_{s,n}^\dagger e^{i\triangle kz_0} |0\rangle, \qquad (2)$$

in which $\hat{a}_{s,n}^\dagger$ and $\hat{a}_{i,m}^\dagger$ are generation operators of signal (s) and idle (i) photons along n- and m-polarizations, respectively;

$\zeta_{lmn}(\theta, \alpha_j, z_0) \propto \chi^{(2)}_{lmn}(\alpha_j, z_0) E_{p,l}(\theta, \alpha_j, z_0)$ is the nonlinear conversion coefficient which is proportional to the second-order nonlinear susceptibility of the material $\chi^{(2)}_{lmn}(\alpha_j, z_0)$ and the electric field amplitude of the pump laser along l-polarization $E_{p,l}(\theta, \alpha_j, z_0)$; $\triangle k(\alpha_j, z_0) = k_p(\alpha_j, z_0) - k_s(\alpha_j, z_0) - k_i(\alpha_j, z_0)$ is the wave vector mismatch. θ is the polarization angle of the pump laser; α_j is the twist angle of the corresponding j-th layer around z axis. The overall quantum state of photon pairs generated by multilayer twisted NbOCl$_2$ should be derived by integrating Eq. (2) within the thin-films region:

$$|\Psi(d_1, d_2, \cdots, d_m, \alpha_1, \alpha_2, \cdots, \alpha_m, \theta)\rangle = \int_0^{d_1 + d_2 + \cdots + d_m} \frac{\partial |\psi(\theta, \alpha_j, z)\rangle}{\partial z} dz. \tag{3}$$

where $d_j (j = 1, 2, \cdots, m)$ represents the thicknesses of each stacked layer.

The refractive indices and the second-order nonlinear susceptibility matrix of the j-th layer rotate along with the twist angle:

$$\begin{bmatrix} n_{zz,v} & n_{zx,v} & n_{zy,v} \\ n_{xz,v} & n_{xx,v} & n_{xy,v} \\ n_{yz,v} & n_{yx,v} & n_{yy,v} \end{bmatrix} = \mathbf{R}_n^T(\alpha_j) \begin{bmatrix} n_{a,v} & 0 & 0 \\ 0 & n_{b,v} & 0 \\ 0 & 0 & n_{c,v} \end{bmatrix} \mathbf{R}_n(\alpha_j), \tag{4}$$

$$\chi^{(2)}_j(\alpha_j) = \mathbf{R}_{\chi,\text{ii}}^T(\alpha_j) \chi^{(2)} \mathbf{R}_{\chi,\text{i}}(\alpha_j), \tag{5}$$

where the subscripts x corresponds to H axis and y corresponds to V axis; a, b and c are NbOCl$_2$ crystal axes; $v = p, s, i$ corresponds to pump laser, signal and idle photons, respectively; the superscript T represents the transpose; $\mathbf{R}_n$ is the rotation matrix of the refractive indices, and $\mathbf{R}_{\chi,\text{i}}$, $\mathbf{R}_{\chi,\text{ii}}$ are rotation matrices of the nonlinear susceptibility:

$$\mathbf{R}_n(\alpha_j) = \mathbf{R}_{\chi,\text{ii}}(\alpha_j) = \begin{bmatrix} 1 & 0 & 0 \\ 0 & \cos\alpha_j & \sin\alpha_j \\ 0 & -\sin\alpha_j & \cos\alpha_j \end{bmatrix}, \tag{6}$$

$$\mathbf{R}_{\chi,\text{i}}(\alpha_j) = \begin{bmatrix} 1 & 0 & 0 & 0 & 0 & 0 \\ 0 & \cos^2\alpha_j & \sin^2\alpha_j & \sin\alpha_j \cos\alpha_j & 0 & 0 \\ 0 & \sin^2\alpha_j & \cos^2\alpha_j & -\sin\alpha_j \cos\alpha_j & 0 & 0 \\ 0 & -\sin 2\alpha_j & \sin 2\alpha_j & \cos 2\alpha_j & 0 & 0 \\ 0 & 0 & 0 & 0 & \cos\alpha_j & -\sin\alpha_j \\ 0 & 0 & 0 & 0 & \sin\alpha_j & \cos\alpha_j \end{bmatrix}. \tag{7}$$

Specifically, for orthogonally stacked bilayers, we set $\alpha_1 = 0°$ and $\alpha_2 = 90°$; for arbitrary-angle twisted bilayers (Supplementary Fig. S11), α_1 is set to $0°$ and α_2 is swept from $0°$ to $180°$; for tri-layer stacked thin films configuration (Supplementary Figs. S12 and S13), we fixed $\alpha_1 = 0°$ and $\alpha_3 = 90°$, then also twisted the second layer α_2 from $0°$ to $180°$.

The generated entangled states in Eq. (3) can be written using four orthogonal polarization bases:

$$|\Psi\rangle = \frac{a_1 e^{i\phi_1}|HH\rangle + a_2 e^{i\phi_2}|VV\rangle + a_3 e^{i\phi_3}|HV\rangle + a_4 e^{i\phi_4}|VH\rangle}{\sqrt{|a_1|^2 + |a_2|^2 + |a_3|^2 + |a_4|^2}} \tag{8}$$

The density matrix of the state is $\rho = |\Psi\rangle\langle\Psi|$. Then, by introducing a non-Hermitian matrix $\mathbf{R} = \rho\sigma\rho^T\sigma$, where

$$\sigma = \begin{pmatrix} 0 & 0 & 0 & -1 \\ 0 & 0 & 1 & 0 \\ 0 & 1 & 0 & 0 \\ -1 & 0 & 0 & 0 \end{pmatrix}, \tag{9}$$

the concurrence of the state can be determined by[52]:

$$C = \max\{0, \sqrt{r_1} - \sqrt{r_2} - \sqrt{r_3} - \sqrt{r_4}\}, \tag{10}$$

in which $r_1 \geq r_2 \geq r_3 \geq r_4$ are eigenvalues of $\mathbf{R}$ in decreasing order. The fidelity of the generated entangled state can be derived by[53]:

$$F^{\pm} = \text{Tr}(\rho|\Phi^{\pm}\rangle\langle\Phi^{\pm}|), \tag{11}$$

where $|\Phi^{\pm}\rangle = 1/\sqrt{2}(|HH\rangle \pm |VV\rangle)$ are the Bell states.

For the qutrit characterization of tri-layer stacks, we replaced the state definition Eq. (8) as:

$$|\Psi_t\rangle = \frac{a_1 e^{i\phi_1}|HH\rangle + a_2 e^{i\phi_2}|VV\rangle + a_3 e^{i\phi_3}|\xi\rangle}{\sqrt{|a_1|^2 + |a_2|^2 + |a_3|^2}}, \tag{12}$$

in which $|\xi\rangle = 1/\sqrt{2}(|HV\rangle + |VH\rangle)$. And in this case, $|\Phi^{\pm}\rangle$ is replaced by the qutrit state $|\Phi_t^+\rangle = 1/\sqrt{3}(|HH\rangle + |VV\rangle + |\xi\rangle)$ in Eq. (11) to determine the fidelity $|F_t^+\rangle$ of the generated qutrit.

Data availability
All relevant data are available in the main text and Supporting Information, and can be obtained from the authors upon request.

References
1. Kwiat, P. G. et al. New high-intensity source of polarization-entangled photon pairs. *Phys. Rev. Lett.* **75**, 4337–4341 (1995).
2. Wang, J., Sciarrino, F., Laing, A. & Thompson, M. G. Integrated photonic quantum technologies. *Nat. Photonics* **14**, 273–284 (2019).
3. Wang, Y., Jons, K. D. & Sun, Z. Integrated photon-pair sources with nonlinear optics. *Appl. Phys. Rev.* **8**, 011314 (2021).
4. Pelucchi, E. et al. The potential and global outlook of integrated photonics for quantum technologies. *Nat. Rev. Phys.* **4**, 194–208 (2021).
5. Kwiat, P. G., Waks, E., White, A. G., Appelbaum, I. & Eberhard, P. H. Ultrabright source of polarization-entangled photons. *Phys. Rev. A* **60**, R773–R776 (1999).
6. Bitton, G., Grice, W. P., Moreau, J. & Zhang, L. Cascaded ultrabright source of polarization-entangled photons. *Phys. Rev. A* **65**, 063805 (2002).
7. Dousse, A. et al. Ultrabright source of entangled photon pairs. *Nature* **466**, 217–220 (2010).
8. Jin, H. et al. On-chip generation and manipulation of entangled photons based on reconfigurable lithium-niobate waveguide circuits. *Phys. Rev. Lett.* **113**, 103601 (2014).
9. Solntsev, A. S., Kumar, P., Pertsch, T., Sukhorukov, A. A. & Setzpfandt, F. LiNbO$_3$ waveguides for integrated SPDC spectroscopy. *APL Photonics* **3**, 021301 (2018).
10. Zhao, J., Ma, C., Rusing, M. & Mookherjea, S. High quality entangled photon pair generation in periodically poled thin-film lithium niobate waveguides. *Phys. Rev. Lett.* **124**, 163603 (2020).
11. Javid, U. A. et al. Ultrabroadband entangled photons on a nanophotonic chip. *Phys. Rev. Lett.* **127**, 183601 (2021).
12. Guo, X. et al. Parametric down-conversion photon-pair source on a nanophotonic chip. *Light. Sci. Appl.* **6**, e16249 (2017).

13. Okoth, C., Cavanna, A., Santiago-Cruz, T. & Chekhova, M. V. Microscale generation of entangled photons without momentum conservation. *Phys. Rev. Lett.* **123**, 263602 (2019).

14. Sun, C. W. et al. Compact polarization-entangled photon-pair source based on a dual-periodically-poled Ti: LiNbO₃ waveguide. *Opt. Lett.* **44**, 5598–5601 (2019).

15. Santiago-Cruz, T. et al. Photon pairs from resonant metasurfaces. *Nano Lett.* **21**, 4423–4429 (2021).

16. Xue, G.-T. et al. Ultrabright multiplexed energy-time-entangled photon generation from lithium niobate on insulator chip. *Phys. Rev. Appl.* **15**, 064059 (2021).

17. Sultanov, V. & Chekhova, M. Temporally distilled high-dimensional biphotonic states from thin sources. *ACS Photonics* **11**, 2–6 (2023).

18. Santiago-Cruz, T. et al. Resonant metasurfaces for generating complex quantum states. *Science* **377**, 5 (2022).

19. Xia, F., Wang, H., Xiao, D., Dubey, M. & Ramasubramaniam, A. Two-dimensional material nanophotonics. *Nat. Photonics* **8**, 899–907 (2014).

20. Yin, X. et al. Edge nonlinear optics on a MoS₂ atomic monolayer. *Science* **344**, 488–490(2014).

21. Autere, A. et al. Nonlinear optics with 2D layered materials. *Adv. Mater.* **30**, e1705963 (2018).

22. Cao, Y. et al. Unconventional superconductivity in magic-angle graphene superlattices. *Nature* **556**, 43–50 (2018).

23. Cao, Y. et al. Correlated insulator behaviour at half-filling in magic-angle graphene superlattices. *Nature* **556**, 80–84 (2018).

24. Seyler, K. L. et al. Signatures of moire-trapped valley excitons in MoSe₂/WSe₂ heterobilayers. *Nature* **567**, 66–70 (2019).

25. Du, L. et al. Moire photonics and optoelectronics. *Science* **379**, eadg0014 (2023).

26. Kim, B. et al. Three-dimensional nonlinear optical materials from twisted two-dimensional van der Waals interfaces. *Nat. Photonics* **18**, 91–98 (2023).

27. Baek, H. et al. Highly energy-tunable quantum light from moiré-trapped excitons. *Sci. Adv.* **6**, eaba8526 (2020).

28. Guo, Q. et al. Ultrathin quantum light source with van der Waals NbOCl₂ crystal. *Nature* **613**, 53–59 (2023).

29. Sultanov, V., Santiago-Cruz, T. & Chekhova, M. V. Flat-optics generation of broadband photon pairs with tunable polarization entanglement. *Opt. Lett.* **47**, 3872–3875 (2022).

30. Ma, J. et al. Polarization engineering of entangled photons from a lithium niobate nonlinear metasurface. *Nano Lett.* **23**, 8091–8098 (2023).

31. Zhang, J. et al. Spatially entangled photon pairs from lithium niobate nonlocal metasurfaces. *Sci. Adv.* **8**, eabq4240 (2022).

32. Sultanov, V. et al. Tunable entangled photon-pair generation in a liquid crystal. *Nature* https://doi.org/10.1038/s41586-024-07543-5 2024.

33. Santos, E. A. et al. Entangled photon-pair generation in nonlinear thin-films. *Nanophotonics* https://doi.org/10.1515/nanoph-2024-0111 2024.

34. Weissflog, M. A. et al. Nonlinear nanoresonators for Bell state generation. *Apply. Phys. Rev.* **11**, 011403 (2024).

35. Weissflog, M. A. et al. A tunable transition metal dichalcogenide entangled photon-pair source. *Nat. Commun.* **15**, 7600 (2024).

36. Modlawska, J. & Grudka, A. Nonmaximally entangled states can be better for multiple linear optical teleportation. *Phys. Rev. Lett.* **100**, 110503 (2008).

37. Christensen, G. G. et al. Detection-loophole-free test of quantum nonlocality, and applications. *Phys. Rev. Lett.* **111**, 130406 (2013).

38. White, A. G. et al. Nonmaximally entangled states: prduction, characterization, and utilization. *Phys. Rev. Lett.* **83**, 3103 (1999).

39. Ecker, S., Sohr, P., Bulla, L., Ursin, R. & Bohmann, M. Remotely estanlishing polarization entanglement over noisy polarization channels. *Phys. Rev. Appl.* **17**, 034009 (2022).

40. Braun, D. et al. Quantum-enhanced measurements without entanglement. *Rev. Mod. Phys.* **90**, 035006 (2018).

41. Datta, A. et al. Quantum metrology with imperfect states and detectors. *Phys. Rev. A* **83**, 063836 (2011).

42. Friis, N., Vitagliano, G., Malik, M. & Huber, M. Entanglement certification from theory to experiment. *Nat. Rev. Phys.* **1**, 72–87 (2019).

43. Elshaari, A. W., Pernice, W., Srinivasan, K., Benson, O. & Zwiller, V. Hybrid integrated quantum photonic circuits. *Nat. Photonics* **14**, 285–298 (2020).

44. Li, L. et al. Metalens-array–based high-dimensional and multiphoton quantum source. *Science* **368**, 4 (2020).

45. Ding, F. & Bozhevolnyi, S. I. Advances in quantum meta-optics. *Mater. Today* **71**, 63–72 (2023).

46. Lanyon, B. P. et al. Manipulating biphotonic qutrits. *Phys. Rev. Lett.* **100**, 060504 (2008).

47. Guo, Q. et al. Colossal in-plane optical anisotropy in a two-dimensional van der Waals crystal. *Nat. Photonics* **18**, 1170–1175 (2024).

48. Hong, C. K. & Mandel, L. Theory of parametric frequency down conversion of light. *Phys. Rev. A* **31**, 2409 (1985).

49. Keller, T. E. & Rubin, M. H. Theory of two-photon entanglement for spontaneous parametric down-conversion driven by a narrow pump pulse. *Phys. Rev. A* **56**, 1534 (1997).

50. Boyd, R. W. *Nonlinear Optics* 4th edn (Academic Press, 2020).

51. Basset, M. G. et al. Video-rate imaging with undetected photons. *Laser Photon. Rev.* **15**, 2000327 (2021).

52. James, D. F. V. et al. Measurement of qubits. *Phys. Rev. A* **64**, 052312 (2001).

53. Walls, D. F. & Milburn, G. J. *Quantum Optics* 2nd edn (Springer, 2008).

Acknowledgements

Author contributions

Q.G. conceived and coordinated this work. Q.G. and Q.Z. synthesized the crystals, conducted structural and optical characterizations. Q.G. fabricated all the samples for experiments. Y.K.W., G.C.G., and X.F.R. conducted the SHG and SPDC experiments. D.Z. and A.A. did the SPDC theoretical modeling on stacked samples. Q.G. analyzed the data and wrote the manuscript. All authors discussed the results and contributed to the manuscript. Q.G. and C.W.Q. supervised the project.

Competing interests

The authors declare no competing interests.

Additional information

Supplementary information The online version contains supplementary material available at https://doi.org/10.1038/s41467-024-54876-w.

Correspondence and requests for materials should be addressed to Qiangbing Guo, Xi-Feng Ren or Cheng-Wei Qiu.

Reprints and permissions information is available at http://www.nature.com/reprints

Publisher's note Springer Nature remains neutral with regard to jurisdictional claims in published maps and institutional affiliations.